NUMERICAL STUDY OF ROUGHNESS MODEL EFFECT AT ACTUAL SHIP SCALE

KUNIHIDE OHASHI*

*National Maritime Research Institute
6-38-1 Shinkawa, Mitaka, Tokyo, Japan
e-mail: k-ohashi@nmri.go.jp

Key words: Surface Roughness, Actual Ship Scale

Abstract. Numerical study of roughness effects at an actual ship scale is performed. The roughness models which are based on the two equation turbulence model are employed. First, the roughness models are examined on the 2D flat plate case at the Reynolds numbers 1.0×10^8 and 1.0×10^9. The resistance coefficient increases with the roughness height, and the uncertainty analysis about the resistance coefficient is performed. Additionally, the distributions of the non-dimensional velocities u^+ based on the non-dimensional heights y^+ are compared with changing the roughness height. Next, the roughness models are applied to the flows around a ship in the actual scale. The velocity contours are compared with the measured results on the actual ship. The results with the roughness models show the good agreement comparing with the smooth surface condition.

1 INTRODUCTION

Numerical study about the roughness effect at the actual ship scale is performed. The roughness models on the two equation turbulence model are employed. Computations of flows around a flat plate corresponding to an actual ship scale are selected as the fundamental test case, and detailed analysis is carried out. Next, the present method is applied to the flows around the ship which has the measured data on the actual sea test. The roughness effect is revealed through the comparisons on the case with/without the roughness model and the measured data.

2 COMPUTATIONAL METHOD

2.1 Base solver

An in-house structured CFD solver [1] is employed. The governing equation is 3D RANS equation for incompressible flows. Artificial compressibility approach is used for the velocity-pressure coupling. Spatial discretization is based on a finite-volume method. A cell centered layout is adopted in which flow variables are defined at the centroid of each cell and a control volume is a cell itself. Inviscid fluxes are evaluated by the third-order upwind scheme based on the flux-difference splitting of Roe. The evaluation of viscous fluxes is second-order accurate.

The first order Euler implicit scheme is employed for the temporal step. The linear equation system is solved by the symmetric Gauss-Seidel (SGS) method.

For free surface treatment, an interface capturing method with a single phase level set approach is employed. The propeller effects are accounted for according to the body forces derived from the propeller model[1], which is based on the potential theory.

2.2 Overset-grid method

The weight values for the overset-grid interpolation are determined by an in-house system[2]. The detail of the system can be found on [2], the summary is described.

1. The priority of the computational grid is set.
2. The cells of a lower priority grid and inside a body is identified (called as in-wall cell in here).
3. Receptors cells which the flow variables have to be interpolated from donor cells are defined. Two cells on a higher priority grid and facing to the outer boundary are set as receptor cells to satisfy the third order discretization of NS solver. Additionally, two cells neighborhood of in-wall cells, the cells of a lower priority grid and inside the domain of a higher priority grid are also set as the receptor cell.
4. The weight values for the overset interpolation are determined by solving the inverse problem based on Ferguson spline interpolation.

Flow variables of the receptor cell are updated when the boundary condition is set. The forces and moments are integrated on the higher priority grid to eliminate the lapped region on body surfaces. At first, the cell face of the lower priority grid is divided into small pieces. Secondly, the small piece is projected to the cell face of the higher priority grid by using the normal vector of the higher priority face. Then the 2D solid angle is computed and the small piece is decided in or out of the higher priority face. Once the small piece is in the higher priority face, the area ratio of the piece is set to zero. Finally, the area ratio is integrated on the lower priority face, then we have the ratio to integrate the forces and moments on lower priority face.

2.3 Roughness model

Roughness effects are taken into account by the roughness models based on the two models. The model which is proposed by Wilcox [3][4] is named as Model1, and the model which is proposed by Hellsten [5] is named as Model2 in hereafter. Non-dimensionalized roughness height is defined by using frictional velocity u_τ and roughness height h_r as follows:

$$h_r^+ = \frac{u_\tau h_r}{\nu} \tag{1}$$

Non-dimensionalized form of Eq.(1) is given as follows:

$$h_r^+ = u_\tau h_r R \tag{2}$$

Non-dimensionalized roughness height is limited $h_r^+ < 400$ in Model1 and the function S_R is introduced.

$$S_R = \begin{cases} \left(\frac{200}{max(h_R^+, h_{min}^+)}\right)^2 & h_R^+ \leq 5 \\ \frac{100}{h_R^+} + \left[\left(\frac{200}{h_R^+}\right)^2 - \frac{100}{h_R^+}\right] e^{5-h_R^+} & h_R^+ > 5 \end{cases} \tag{3}$$

where the new variable h_{min}^+ is employed above equation based on the Model2 which is proposed by Hellsten to ensure the function to the smooth surface condition, and h_{min}^+ is defined as $h_{min}^+ = 9.6 y_1^{+0.85}$ which is based on the first computational cell adjacent to the wall surface and non-dimensionalzed height y_1^+.

The function S_R is introduced by the Model2 as follows:

$$S_R = \begin{cases} \left(\frac{50}{max(h_R^+, h_{min}^+)}\right)^2 & h_R^+ < 25 \\ \frac{100}{h_R^+} & h_R^+ \geq 25 \end{cases} \tag{4}$$

where $h_{min}^+ = 2.4 y_1^{+0.85}$ is applied.

The boundary condition of ω on a wall surface is given as follows:

$$\omega = \frac{u_\tau^2}{\nu} S_R \tag{5}$$

Non-dimensionalized form of Eq.(5) is given as follows:

$$\omega = u_\tau^2 S_R R \tag{6}$$

The reference velocity profile which is proposed by Apsley[6] is used in the present study.

$$u^+ = y_{v0}^+ + \frac{1}{\kappa} ln\left(\frac{1 + \kappa(y^+ - y_v^+)}{1 + \kappa(y_{v0}^+ - y_v^+)}\right) \tag{7}$$

$$y_v^+ = \begin{cases} C - \frac{1}{\kappa} ln(\kappa) & C - \frac{1}{\kappa} ln(\kappa) \geq 0 \\ \frac{1}{\kappa}(1 - e^{-\kappa(C - \frac{1}{\kappa} ln(\kappa))}) & C - \frac{1}{\kappa} ln(\kappa) < 0 \end{cases} \tag{8}$$

$$C = 8 - \frac{1}{\kappa} ln(h_R^+ + 3.152) \tag{9}$$

$$y_{v0}^+ = max(y_v^+, 0) \tag{10}$$

where κ is assumed as 0.41.

2.4 Uncertainty analysis

Uncertainty analysis based on the Richardson extrapolation method with the FS method[7] is performed. The grid discretization uncertainty is evaluated due the steady condition on the present study, and the three systematic grids with the uniform refinement ratio $r_G = \sqrt{2}$ are utilized. Once, the solutions $S_3,\ S_2,\ S_1$ relevant from the coarse grid to fine grid are obtained, the solution changes are defined as $\epsilon_{12} = S_2 - S_1,\ \epsilon_{23} = S_3 - S_2$. The convergence ratio R is $\epsilon_{12}/\epsilon_{23}$, and R takes the monotonic convergence with $0 < \epsilon_{12}/\epsilon_{23} < 1$. The order of accuracy p and the error δ_{RE} are defined as follows:

$$p = \frac{ln(\epsilon_{23}/\epsilon_{12})}{ln(r_G)},\ \ \delta_{RE} = S_1 - S_0 = \frac{\epsilon_{12}}{r_G^p - 1} \tag{11}$$

The uncertainty is estimated by the following equation using the variable $P = p/p_{th}$. Theoretical accuracy p_{th} is assumed $p_{th} = 2$.

$$U_{SN} = \begin{cases} (2.45 - 0.85P)|\delta_{RE}|, & 0 < P \leq 1 \\ (16.4P - 14.8)|\delta_{RE}|, & P > 1 \end{cases} \tag{12}$$

3 COMPUTED RESULTS

3.1 2D Flat plate case

A 2D flat plate case is selected as the fundamental test case. The Reynolds number is set 1.0×10^8 and 1.0×10^9 based on the plate length L as the reference length. Table 1 shows the computational grids with the three resolutions. The space between the first cell center and wall surface satisfies $y^+ \leq 1$. Fig.1 shows the computational grid of the medium grid, the boundary conditions and the definitions of directions of the divisions. The distance between the wall surface and the top boundary is 0.1L.

Table 1: Division number of computational grid

Grid	IM×JM
Coarse(G_3)	137×81
Medium(G_2)	193×113
Fine(G_1)	273×161

The value which is estimated by the empirical formula [8] utilized for the reference.

$$C_D = \left(2.635 + 0.618 ln \frac{L}{h_r}\right)^{-2.57} \tag{13}$$

Table 2 shows the comparison of the resistance coefficients of model1 with changing the roughness height from $h_r = 1 \times 10^{-6}$ to $h_r = 7.5 \times 10^{-6}$ and the grid resolutions at the Reynolds number $R = 1.0 \times 10^8$. The roughness height is non-dimensionalized by the plate length L, and the roughness height is selected in the range where the resistance coefficient becomes larger than

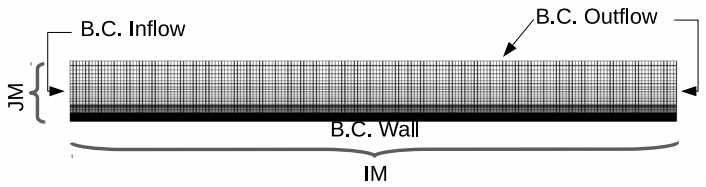

Figure 1: Computational grid(Medium grid)

the value of the smooth surface. The uncertainty is resulted in the range from 1% to 3% of the solution of the fine grid, thus, the uncertainty takes small value using the present computational grids. Although the computed results are slightly higher than the value of the empirical formula, the resistance coefficient increase with the roughness height. Table 2 shows similar results with the model2. The uncertainty is about 1% to 3% of the solution of the fine grid. Comparing between the results of model1 and model2, the resistance coefficient of model2 becomes larger than the value of model1 at $h_r = 1 \times 10^{-6}$, and the values of model2 takes smaller value than the results of model1 at 2.5×10^{-6} and 5×10^{-6}. The results of model1 and model2 are same at 7.5×10^{-6}.

Figure 2 shows the comparisons of the non-dimensionalized velocity u^+ and non-dimensionalized distance y^+ of model2 at the positions $x/L = 0.5$ and $x/L = 0.9$. The results of model1 are the same as the results of model2, then, the results of model1 are omitted. For the reference, the correlations based on the smooth surface condition and Eq.(7) with the roughness $h_r = 7.5 \times 10^{-6}$ are also shown in Figure 2. The velocity distributions change and become slower in the logarithmic region with the roughness height. The difference due to the roughness height seems small in the viscous sublayer region. The velocities at $x/L = 0.5$ and $x/L = 0.9$ take the same distribution in the logarithmic region, and the difference can be found in the outer region.

Table 2: Resistance coefficient (Model1,$R = 1.0 \times 10^8$)

Grid	Smooth	1×10^{-6}	2.5×10^{-6}	5×10^{-6}	7.5×10^{-6}
Coarse	2.062	2.074	2.307	2.618	2.734
Medium	2.096	2.119	2.374	2.686	2.808
Fine	2.108	2.130	2.382	2.696	2.818
$U_{SN}\%G_1$	3.06	3.10	1.62	1.95	1.81
Emp.	—	2.024	2.313	2.572	2.742

Table 4 shows the results of model1 at $R = 1.0 \times 10^9$ with changing the non-dimensionalized roughness height from $h_r = 1 \times 10^{-7}$ to $h_r = 7.5 \times 10^{-7}$. The roughness height is selected in the range where the resistance coefficient becomes larger than the value of the smooth surface. The uncertainty becomes smaller than the values of the Reynolds number $R = 1.0 \times 10^8$, and the resistance coefficient takes similar value of the empirical formula. Table 5 shows the results of model2. The resistance coefficient of model2 takes larger value than the results of model1 in the range until $h_r = 2.5 \times 10^{-7}$, then, the relation shows the opposite trend.

Table 3: Resistance coefficient (Model2,$R = 1.0 \times 10^8$)

Grid	Smooth	1×10^{-6}	2.5×10^{-6}	5×10^{-6}	7.5×10^{-6}
Coarse	2.062	2.149	2.286	2.526	2.734
Medium	2.096	2.197	2.342	2.597	2.808
Fine	2.108	2.208	2.352	2.606	2.818
$U_{SN}\%G_1$	3.06	2.97	2.40	1.71	1.81
Emp.	—	2.024	2.313	2.572	2.742

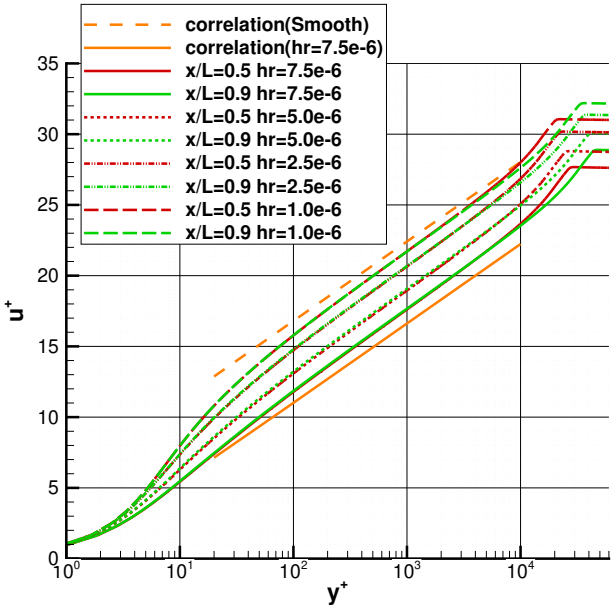

Figure 2: Comparison of y^+ and u^+ at $R = 1.0 \times 10^8$ (Model2)

Figure 3 shows the distributions based on u^+ and y^+. For the reference, the correlation based on Eq.(7) at $h_r = 7.5 \times 10^{-7}$ is shown. The computed results show the similar distribution with the case $R = 1.0 \times 10^8$ excepting the logarithmic region becomes wider than the results of $R = 1.0 \times 10^8$.

Figure 4 shows the distribution of h_r^+ on the flat plate at the condition with $h_r = 7.5 \times 10^{-7}$. h_r^+ takes larger value near the front end of the flat plate, then, the value becomes almost constant value with $h_r^+ = 25$, and the value is within the model limitation $h_r^+ < 400$.

3.2 Actual ship scale

The numerical study with/without the roughness effect is performed on the case with the tanker hull[9] which has the flow measurement data on the actual ship. The computations are carried out on the propulsive condition with the free surface effect. The Reynolds number based

Table 4: Resistance coefficient (Model1,$R = 1.0 \times 10^9$)

Grid	Smooth	1×10^{-7}	2.5×10^{-7}	5×10^{-7}	7.5×10^{-7}
Coarse	1.538	1.553	1.635	1.878	1.952
Medium	1.565	1.580	1.669	1.917	1.994
Fine	1.571	1.586	1.673	1.922	1.998
$U_{SN}\%G_1$	0.17	2.25	1.14	1.29	0.86
Emp.	—	1.487	1.673	1.837	1.944

Table 5: Resistance coefficient (Model2,$R = 1.0 \times 10^9$)

Grid	Smooth	1×10^{-7}	2.5×10^{-7}	5×10^{-7}	7.5×10^{-7}
Coarse	1.538	1.593	1.672	1.802	1.936
Medium	1.565	1.621	1.704	1.840	1.980
Fine	1.571	1.627	1.709	1.845	1.984
$U_{SN}\%G_1$	0.17	2.18	1.58	1.36	0.85
Emp.	—	1.487	1.673	1.837	1.944

on the ship length L is $R = 2.43 \times 10^9$, and the Froude number is $Fn = 0.153$. Propulsive condition is achieved by using the propeller model[1]. The propeller rotational speed and thrust is adjusted to be equal to the resistance of the ship. The roughness value is set $150 \times 10^{-6}m$ based on the ITTC recommended procedure[10].

Table 6 shows the division number of computational grids in each direction. The grids are arranged with the priority of the overset interpolation. The computational grid is consisted from the hull grid, the rudder grid and two rectangular grids including the refinement grid near the aft part of the ship hull and the grid covering the whole domain. The division numbers of the hull and rudder grids are altered to examine the effect of the grid resolution with reference to the 2D flat plate case.

Figure 5 shows the global view of the computational grids with the boundary conditions and the grids near the aft part of the ship. The space between the first cell center and wall surface also satisfies $y^+ \leq 1$.

Table 6: Division number of computational grid

Grid	Coarse	Medium	Fine
	IM×JM×KM	IM×JM×KM	IM×JM×KM
Rudder	45×69×35	61×97×49	85×137×69
Refined Rect.	45×33×45	45×33×45	45×33×45
Hull	141×145×65	197×209×89	277×305×125
Rect.	337×89×57	337×89×57	337×89×57

Figure 6 shows the axial velocity contour with/without the roughness effect at the propeller plane on the towing condition. The results based on the three grid are also shown. The region which the axial velocity is lower than 0.3 spreads corresponding to the grid resolution. The axial

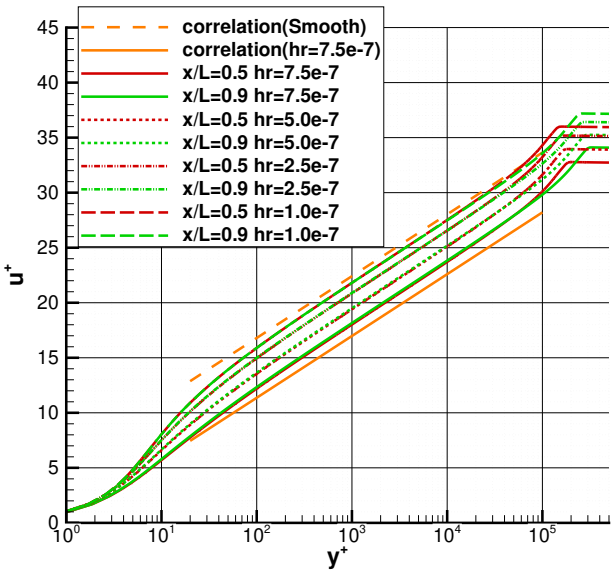

Figure 3: Comparison of y^+ and u^+ at $R = 1.0 \times 10^9$ (Model2)

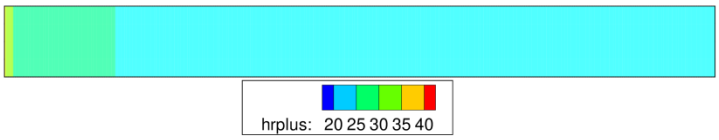

Figure 4: Non-dimensional roughness on the plate at $R = 1.0 \times 10^9$ (Model2)

velocity with the roughness effect becomes lower than the value of the smooth surface condition, and the difference between the roughness models is slightly small.

Figure 7 shows the comparisons with the measured data at the actual ship. The position is x/L=0.98533 from the fore perpendicular position. The results with the roughness effect show agreement with the measured data, especially, the range $u/U = 0.5 - 0.7$. The differences between the result of the grid resolutions are slightly small, and the differences between the result of model1 and model2 can be negligible.

Figure 8 shows the distribution of the non-dimensionalized roughness height h_r^+ on the body surfaces. h_r^+ takes small value near the fore and stern end, and h_r^+ is distributed on the body surface with the value near 40. The difference between the port and starboard sides is slightly small. The non-dimensionalized roughness height on the rudder surface which is positioned behind the propeller takes higher value than h_r^+ on the hull surface. The difference between the port and starboard sides on the rudder surface can be observed which is affected by the propeller rotational flow. The velocities of the two models have the identical lines.

Finally, the distribution of the non-dimensional velocity u^+ at the bottom of the hull and midship $x/L = 0$ and center line $y/L = 0$ is shown is Figure 9. The correlation based on Eq.(7) is also shown in Figure 9. The non-dimensional velocities with the roughness models decreases

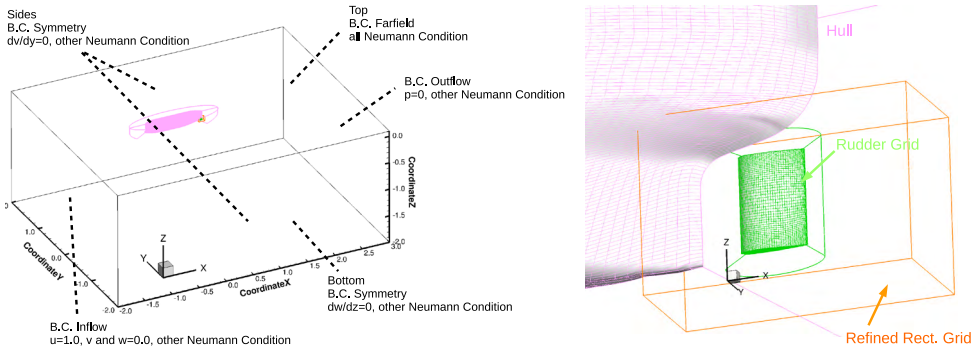

Figure 5: Computational grids(left:global view, right:near aft part of hull)

comparing with the velocity of the smooth surface condition. The non-dimensional velocities with the roughness are decreased by the rise of frictional velocity due the roughness effect. The difference between the roughness models is negligible.

4 CONCLUSIONS

- The two roughness models based on $k-\omega SST$ model are introduced to examined the roughness effect on the actual ship scale.
- The 2D flat plate case is selected as the fundamental test case, and the comparisons of the resistance coefficient and uncertainty analysis are performed.
- The effect of the roughness model is examined at the case with the tanker hull which has the the flow measurement data on the actual ship, and the axial flows behind the ship hull are decelerated by the roughness effect.
- The computed results with the roughness effect show good agreement with the measured data on the actual ship.

REFERENCES

[1] K. Ohashi et al., Development of a structured overset Navier-Stokes solver including a moving grid with a full multigrid method, J. Mar. Sci. Tech., 2018.

[2] H. Kobayashi and Y. Kodama, Developing Spline Based Overset Grid Assembling Approach and Application to Unsteady Flow Around a Moving Body, Journal of Mathematics and System Science 6, pp.339-347, 2016

[3] D.C. Wilcox, Turbulence modeling for CFD, Third Edition, DCW Industries, 2006.

[4] L. Eça, M. Hoekstra, Numerical aspects of including wall roughness effects in the SST $k-\omega$ eddy-viscosity turbulence model, Comp. and Fluids, Vol.40, pp.299-314, 2011.

[5] A. Hellsten., Some improvements in Menter's $k-\omega$ SST AIAA-98-2554, 1997.

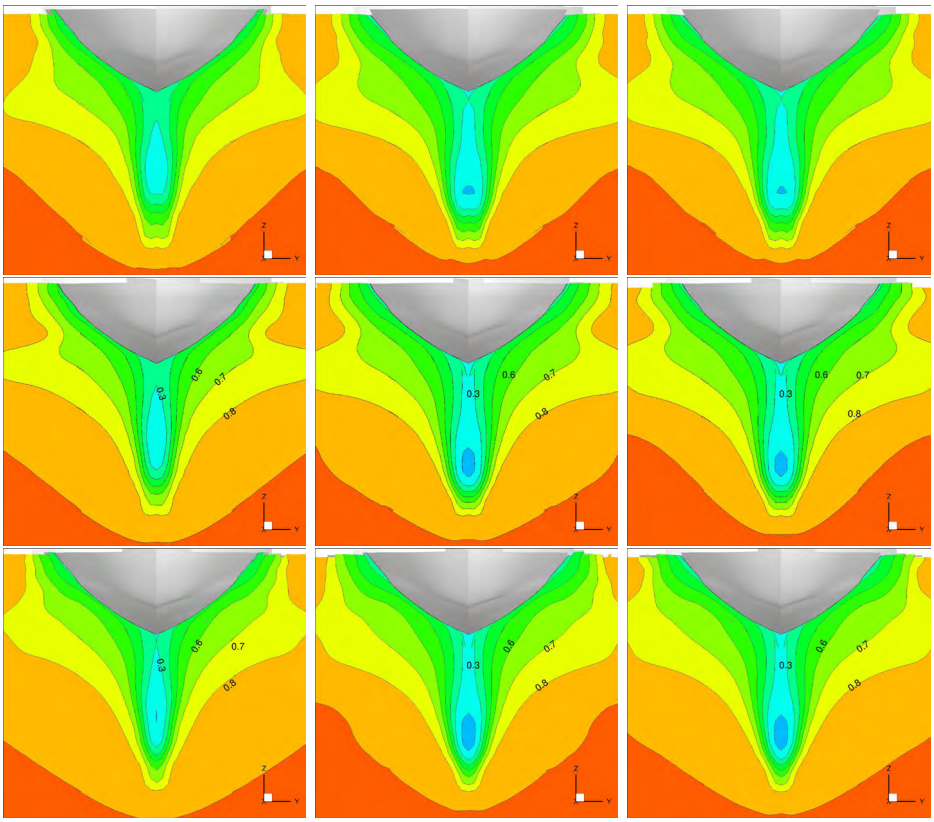

Figure 6: Axial velocity contour(Top:Coarse grid, Mid:Medium grid, Bottom:Fine grid)

[6] D. Apsley, CFD calculation turbulent flow with arbitrary wall roughness, Flow Turb. Comb., Vol.78, pp.153-175, 2007.

[7] T. Xing, , F. Stern, Factors of safety for Richardson extrapolation, J. Fluids Eng., Vol.132(6), 2010.

[8] A. Mills, X. Hang, On the skin friction coefficient for a fully rough flat plate, Trans. ASME, J. Fluids Eng., Vol.105, pp.364-365, 1983.

[9] Proc. of CFD Workshop Tokyo 1994

[10] ITTC recommended procedures and Guidelines 7.5-02-03-01.4, 1978 ITTC Performance Prediction Method.

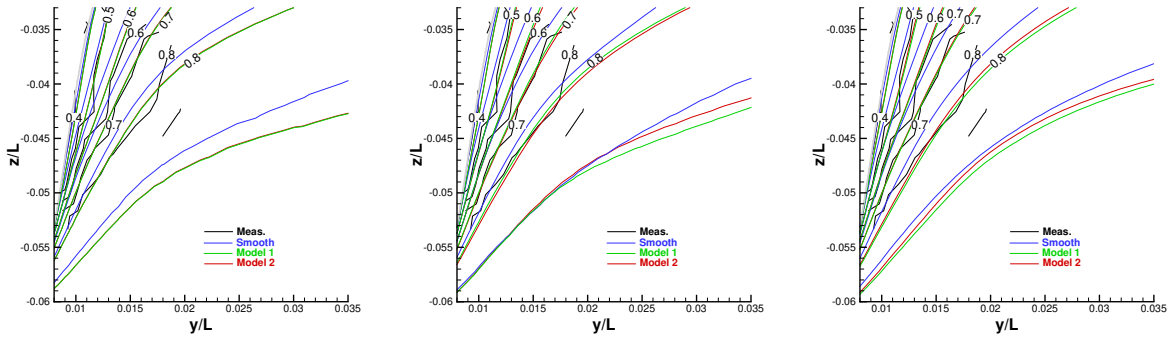

Figure 7: Comparison of velocity contours with measured results (Top:Coarse grid, Mid:Medium grid, Bottom:Fine grid)

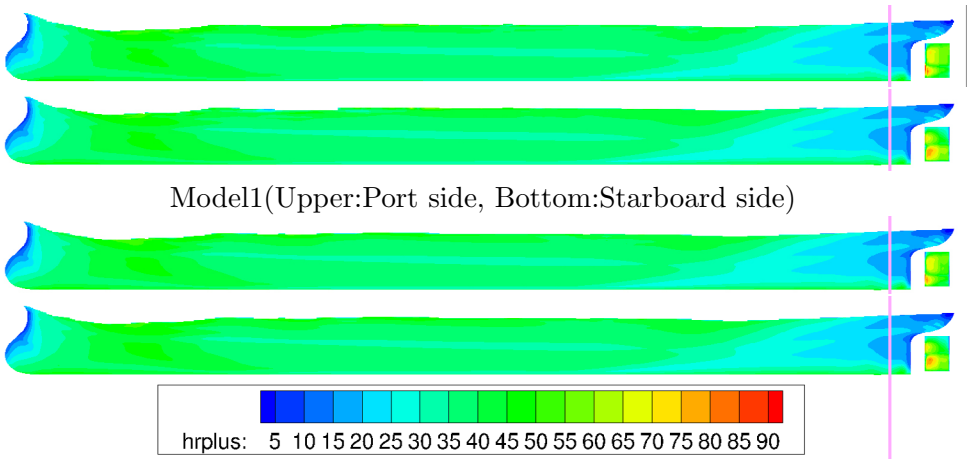

Model1(Upper:Port side, Bottom:Starboard side)

Model2(Upper:Port side, Bottom:Starboard side)

Figure 8: Non-dimensional roughness on the hull and rudder surfaces

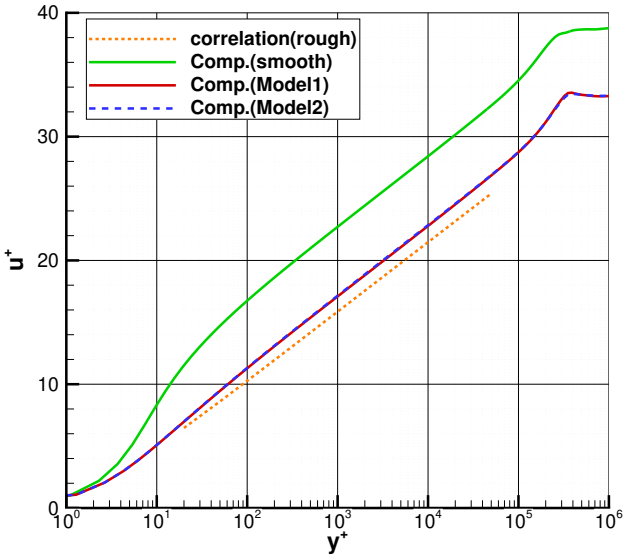

Figure 9: Comparison of y^+ and u^+ at $x/L = 0$ and $y/L = 0$